AIAA JOURNAL
Vol. 46, No. 7, July 2008

Computation of Airfoil–Vortex Interaction Using a Vorticity-Preserving Scheme

Fabrice Falissard* and Alain Lerat†
Ecole Nationale Supérieure d'Arts et Métiers, 75013 Paris, France
and
Jacques Sidès‡
ONERA, 92322 Châtillon, France

DOI: 10.2514/1.33719

We recently proved that a dissipative residual-based scheme of second-order accuracy is vorticity-preserving for the compressible Euler equations. In the present paper, this scheme is extended to curvilinear grids and applied to the computation of the interaction between a Scully vortex and a NACA0012 airfoil at a Mach number of 0.5. A grid convergence study and a comparison with a conventional scheme and with experimental measurements are presented. The new scheme shows a faster grid convergence, especially for the vortex trajectories and deformations during the interaction.

Nomenclature

A, B	=	flux Jacobian matrices
C_p	=	pressure coefficient
c	=	airfoil chord
E	=	specific total energy
F, G	=	numerical flux
f, g	=	physical flux
H	=	specific total enthalpy
M	=	Mach number
p	=	pressure
r	=	residual
$\tilde{r}$	=	discrete residual
S	=	entropy
T	=	temperature
T_A, T_B	=	matrices for diagonalizing A and B
u, v	=	velocity components
$\mathbf{V}$	=	velocity vector
v_θ	=	azimuthal velocity
w	=	conservative variable vector
x, y	=	Cartesian coordinates
Γ	=	circulation
γ	=	isentropic exponent
Δt	=	time step
δx, δy, h	=	spatial steps
δ_1, μ_1, δ_2, μ_2	=	discrete operators
∂_t, ∂_x, ∂_y	=	differential operators
ε	=	truncation error
Λ	=	difference operator
ρ	=	density
$\rho(A)$, $\rho(B)$	=	spectral radii of the Jacobian matrices
Φ_1, Φ_2	=	dissipation matrices
φ_1, φ_2	=	dissipation-matrix eigenvalues
ω	=	vorticity

Received 26 July 2007; revision received 22 November 2007; accepted for publication 13 December 2007.

*Research Engineer, Laboratoire de Simulation Numérique en Mécanique des Fluides, 151 Boulevard de l'Hôpital.
†Professor, Laboratoire de Simulation Numérique en Mécanique des Fluides, 151 Boulevard de l'Hôpital.
‡Research Engineer, Computational Fluid Dynamics and Aeroacoustics, Boite Postale 72.

Introduction

COMPUTING vortices with very little numerical dissipation is a challenge in many computational fluid dynamics problems, starting from the prediction of fine physical phenomena such as the behavior of small scales in turbulence and extending to complex engineering applications such as the flow simulation over complete aircraft or helicopters.

An approach often considered to reduce the numerical diffusion of vortices consists of increasing the order of accuracy, for instance, using high-order centered schemes with spectral filtering [1–4], residual-based compact schemes [5–8], essentially nonoscillatory [9–11] and weighted essentially nonoscillatory [12,13] schemes, or discontinuous Galerkin methods [14–19].

Another point of view has been proposed by Morton and Roe [20] through the concept of vorticity-preserving schemes in pure acoustics. This attractive concept has been extended to the linearized and full Euler equations [21], and the analysis has led to a residual-based vorticity-preserving (RBV) scheme for the full Euler equations. This scheme is second-order-accurate in time and space, and so we refer to it as the RBV2 scheme.

The objective of the present paper is to assess RBV2 with respect to a conventional scheme for an unsteady compressible flow problem involving vorticity effects. The selected problem is the head-on parallel interaction between a Scully vortex [22] and a NACA0012 airfoil at a Mach number of 0.5 and zero incidence, for which experimental data are available [23,24]. It is representative of the parallel interaction between a helicopter rotor blade and the vortex emitted at the tip of a preceding blade, which is at the origin of the blade–vortex-interaction noise. The selected problem involves vortex propagation, shock-wave formation, secondary-vortex creation, and acoustic-wave emission. It is well documented and has been already used to assess various numerical treatments for vortex-flow computation, such as high-order accuracy [23,24], locally structured [25] and unstructured [26,27] mesh refinements, or vorticity confinement [28]. Our computations will be based on the Euler equations, which are relevant for this problem because previous Euler [25,26,28] and Navier–Stokes [23,24,27,28] simulations exhibit very similar solutions.

The paper is organized as follows. In the next section, the residual-based scheme is presented on a Cartesian mesh, its vorticity-preserving property is recalled, and its extension to curvilinear meshes is precisely described. Then the vorticity-preserving capability of the RBV2 scheme is validated through the calculation of basic vortex flows and a comparison with a conventional scheme of the same order of accuracy. Finally, the application to the airfoil–vortex interaction is considered; after an analysis of the flow solution,

a grid convergence study is performed and a comparison is made with other numerical methods and experimental measurements.

Numerical Method

Residual-Based Schemes

We consider unsteady compressible flows governed by the Euler equations:

$$\partial_t w + \partial_x f + \partial_y g = 0 \tag{1}$$

with

$$w = \begin{bmatrix} \rho \\ \rho u \\ \rho v \\ \rho E \end{bmatrix}, \qquad f = \begin{bmatrix} \rho u \\ \rho u^2 + p \\ \rho uv \\ (\rho E + p)u \end{bmatrix}, \qquad g = \begin{bmatrix} \rho v \\ \rho uv \\ \rho v^2 + p \\ (\rho E + p)v \end{bmatrix}$$

where t is the time, x and y are Cartesian space coordinates, ρ is the density, p the pressure, u and v are the components of the fluid velocity $\mathbf{V}$, and E is the specific total energy. The thermodynamic equation of state is the ideal-gas law.

For the numerical solution of system (1), we consider a dissipative conservative scheme classically written as a space-centered approximation to system (1), plus a numerical dissipation (either added or induced by upwinding). In addition, we require the scheme to be "residual-based." This means that the numerical dissipation, as well as the centered part, can be expressed in terms of discrete approximations of the residual:

$$r = \partial_t w + \partial_x f + \partial_y g$$

Residual-based schemes have been considered by Lerat and Corre [5,6] and Corre et al. [7] in a compact formulation. The objective was to obtain high-order accuracy with residual-based compact schemes. Here, our goal is not necessarily to reach a high accuracy, but to avoid any numerical diffusion of the vorticity field. In a recent paper [21], we showed that this can be achieved with a particular residual-based scheme of second-order accuracy that we named RBV2. Contrary to a residual-based compact scheme that uses several approximations of r, RBV2 is based on a single approximation $\tilde{r}$ of r and can thus be written in the simple form:

$$\Lambda \tilde{r} = 0$$

where Λ is a discrete operator.

Let us first present the RBV2 scheme on a Cartesian mesh, then recall the vorticity-preserving property satisfied by RBV2 for the Euler equations and extend the scheme on a general curvilinear mesh.

RBV2 Scheme on a Cartesian Mesh

Consider a Cartesian mesh ($x_j = j\delta x$, $y_k = k\delta y$) and define the difference and average operators:

$$(\delta_1 v)_{j+\frac{1}{2},k} = v_{j+1,k} - v_{j,k}, \qquad (\mu_1 v)_{j+\frac{1}{2},k} = \tfrac{1}{2}(v_{j+1,k} + v_{j,k}),$$
$$(\delta_2 v)_{j,k+\frac{1}{2}} = v_{j,k+1} - v_{j,k}, \qquad (\mu_2 v)_{j,k+\frac{1}{2}} = \tfrac{1}{2}(v_{j,k+1} + v_{j,k})$$

where $2j$ and $2k$ are integers, so that, for instance,

$$(\delta_1 v)_{j,k} = v_{j+\frac{1}{2},k} - v_{j-\frac{1}{2},k},$$
$$(\delta_1 \mu_2 v)_{j+\frac{1}{2},k+\frac{1}{2}} = \tfrac{1}{2}(v_{j+1,k+1} + v_{j+1,k} - v_{j,k+1} - v_{j,k})$$

For the time discretization $t^n = n\Delta t$, we use the three-time-level operator:

$$(\bar{\Delta} v)^{n+1} = \tfrac{3}{2}v^{n+1} - 2v^n + \tfrac{1}{2}v^{n-1} \tag{2}$$

where n is a positive integer. The RBV2 scheme can be written in the conservative form,

$$\left(\mu_1^2\mu_2^2 \frac{\bar{\Delta} w}{\Delta t} + \frac{\delta_1 F}{\delta x} + \frac{\delta_2 G}{\delta y}\right)^{n+1}_{j,k} = 0 \tag{3}$$

with the numerical flux:

$$F^{n+1}_{j+\frac{1}{2},k} = \left(\mu_1\mu_2^2 f - \frac{\delta x}{2}\Phi_1\mu_2\tilde{r}\right)^{n+1}_{j+\frac{1}{2},k}$$
$$G^{n+1}_{j,k+\frac{1}{2}} = \left(\mu_1^2\mu_2 g - \frac{\delta y}{2}\Phi_2\mu_1\tilde{r}\right)^{n+1}_{j,k+\frac{1}{2}} \tag{4}$$

where the discrete residual $\tilde{r}$ is defined on a 2×2 stencil (see Fig. 1) as

$$\tilde{r}^{\,n+1}_{j+\frac{1}{2},k+\frac{1}{2}} = \left(\mu_1\mu_2 \frac{\bar{\Delta} w}{\Delta t} + \frac{\delta_1\mu_2 f}{\delta x} + \frac{\delta_2\mu_1 g}{\delta y}\right)^{n+1}_{j+\frac{1}{2},k+\frac{1}{2}} \tag{5}$$

and where the dissipation matrices Φ_1 and Φ_2 (introducing some upwinding in the scheme) are given [29] by

$$\Phi_1 = T_A \mathrm{diag}[\varphi_1^{(i)}]T_A^{-1}, \qquad \Phi_2 = T_B \mathrm{diag}[\varphi_2^{(i)}]T_B^{-1},$$
$$\varphi_1^{(i)} = \mathrm{sgn}(a^{(i)})\varphi^{(i)}, \qquad \varphi_2^{(i)} = \mathrm{sgn}(b^{(i)})\psi^{(i)},$$
$$\varphi^{(i)} = \min\left(1, \frac{\delta y|a^{(i)}|}{\delta x \rho(B)}\right), \qquad \psi^{(i)} = \min\left(1, \frac{\delta x|b^{(i)}|}{\delta y \rho(A)}\right) \tag{6}$$

where A (respectively, B) denotes the Jacobian matrix $\mathrm{d}f/\mathrm{d}w$ (respectively, $\mathrm{d}g/\mathrm{d}w$); T_A (respectively, T_B) is a matrix diagonalizing A (respectively, B); and the real values $a^{(i)}$, $b^{(i)}$, $\varphi_1^{(i)}$, and $\varphi_2^{(i)}$ denote the ith eigenvalues of the matrices A, B, Φ_1, and Φ_2, respectively. Finally, $\rho(A) = \max_i|a^{(i)}|$ [similarly, for $\rho(B)$]. It is easy to check that RBV2 can be put in the form

$$(\Lambda\tilde{r})^{n+1}_{j,k} = 0 \tag{7}$$

with the operator

$$\Lambda = \mu_1\mu_2 - \tfrac{1}{2}(\delta_1\Phi_1\mu_2 + \delta_2\Phi_2\mu_1)$$

The RBV2 scheme is thus residual-based and defined on a 3×3 stencil, as shown in Fig. 1. The order of accuracy of the RBV2 scheme is given by the truncation error:

$$\varepsilon = r - \frac{\delta x}{2}(\Phi_1 r)_x - \frac{\delta y}{2}(\Phi_2 r)_y + \mathcal{O}(\Delta t^2, \delta x^2, \delta y^2)$$

where r satisfies the exact solution (i.e., $r = 0$), which proves that RBV2 approximates the Euler equation (1) with a second-order accuracy in time and space. A deeper analysis of the truncation error on a square mesh ($\delta x = \delta y = h$) for advection-dominated flows at speed $\mathbf{V}_0$ shows that the second-order error can be minimized by choosing the time step as

$$\Delta t = \frac{1}{2}\frac{h}{|\mathbf{V}_0|} \tag{8}$$

This choice correspond to a Courant–Friedrichs–Lewy (CFL) number equal to $\frac{1}{2}(M_0 + 1)/M_0$, where M_0 is the Mach number based on $|\mathbf{V}_0|$. Note that the optimal CFL number is greater than one for an advection at subsonic speed and increases as M_0 decreases, which is favorable to numerical efficiency.

Vorticity-Preserving

The momentum equation contained in the conservation laws (1) can be written in intrinsic form as

$$\partial_t(\rho\mathbf{V}) + \nabla\cdot(\rho\mathbf{V}\otimes\mathbf{V}) + \nabla p = 0 \tag{9}$$

By taking the curl of Eq. (9), the pressure disappears and we obtain

$$\partial_t\boldsymbol{\Omega} + \nabla\times[\nabla\cdot(\rho\mathbf{V}\otimes\mathbf{V})] = 0 \tag{10}$$

with

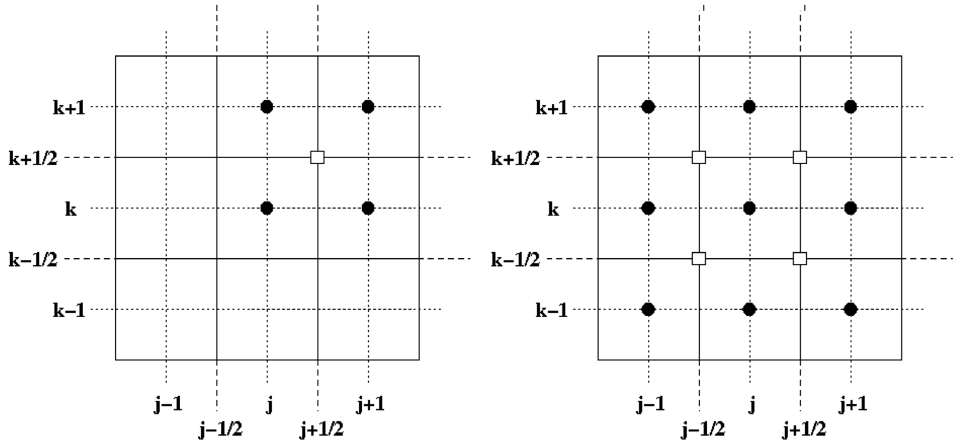

Fig. 1 Stencils of the discrete residual and RBV2 scheme.

$$\mathbf{\Omega} = \nabla \times (\rho \mathbf{V}) = \rho\omega + \nabla\rho \times \mathbf{V} \tag{11}$$

where $\omega = \nabla \times \mathbf{V}$ is the vorticity.

A dissipative conservative scheme is said to be vorticity-preserving for the Euler equations if the numerical solution satisfies a space-centered approximation of Eq. (10). This means that no numerical dissipation or pressure term occurs in the discrete equation of $\mathbf{\Omega}$. It is noteworthy that vorticity-preserving holds for some forms of dissipative conservative schemes and, notably, for RBV2 (see [21] for formal definitions and proofs).

Solution of the Implicit Formulation

The RBV2 scheme is solved using a dual-time technique [30,31]. The unsteady solution is searched as a steady solution of a time-dependent system with respect to a dual time τ:

$$\partial_\tau w + r = 0$$

Practically, the numerical solution $w_{j,k}^{n,m}$ at dual time $\tau^m = m\Delta\tau$ is calculated from

$$\left(\frac{w^{n,m+1} - w^{n,m}}{\Delta\tau}\right)_{j,k} + (\Lambda\tilde{r})_{j,k}^{n,m+1} = 0 \tag{12}$$

and the solution $w_{j,k}^{n+1}$ of Eq. (7) is the steady-state limit of $w_{j,k}^{n,m}$ for large integers m. The Euler backward method in dual time (12) is solved by linearizing $\Lambda\tilde{r}$ and using an alternate-line-symmetric Gauss–Seidel relaxation.

RBV2 Scheme on a Curvilinear Mesh

To satisfy the vorticity-preserving property on curvilinear meshes, it is essential to keep the residual-operator form (7). Again using the dual-time technique (12), we first compute the discrete residual $\tilde{r}$ and then apply the operator Λ. The conservative variables w are defined at the cell centers (j, k) of a structured mesh called the *original mesh*.

Discrete Residual

The residuals are defined in the staggered cells $\mathcal{V}_r = (\mathcal{V}_r)_{j+\frac{1}{2},k+\frac{1}{2}}$, for which the nodes are the cell centers of the original mesh (see Fig. 2):

$$\int_{\mathcal{V}_r} r \,\mathrm{d}\mathcal{V} = \int_{\mathcal{V}_r} (\partial_t w + \partial_x f + \partial_y g)\,\mathrm{d}\mathcal{V}$$
$$= \frac{\mathrm{d}}{\mathrm{d}t}\int_{\mathcal{V}_r} \partial_t w \,\mathrm{d}\mathcal{V} + \int_{\Sigma_r} f_n \,\mathrm{d}\Sigma$$

where Σ_r is the boundary of $\mathcal{V}_r$, $\mathbf{n} = (n_x, n_y)$ is the unit outer normal to Σ_r, and $f_n = f n_x + g n_y$ is the normal density flux.

More precisely, the discrete residuals $\tilde{r}_{j+\frac{1}{2},k+\frac{1}{2}}$ are computed at the centers of the quadrangle cells $(\mathcal{V}_r)_{j+\frac{1}{2},k+\frac{1}{2}}$ with boundary

$$(\Sigma_r)_{j+\frac{1}{2},k+\frac{1}{2}} = (\Gamma_r)_{j+1,k+\frac{1}{2}} \cup (\Gamma_r)_{j,k+\frac{1}{2}} \cup (\Gamma_r)_{j+\frac{1}{2},k+1} \cup (\Gamma_r)_{j+\frac{1}{2},k}$$

using the finite volume formulation:

$$\tilde{r}_{j+\frac{1}{2},k+\frac{1}{2}} = \left(\mu_1\mu_2 \frac{\bar{\Delta}w}{\Delta t}\right)_{j+\frac{1}{2},k+\frac{1}{2}} + \frac{1}{|\mathcal{V}_r|_{j+\frac{1}{2},k+\frac{1}{2}}} \sum_{q=0}^{1} [(|\Gamma_r|\mu_2 f_n)_{j+q,k+\frac{1}{2}}$$
$$+ (|\Gamma_r|\mu_1 f_n)_{j+\frac{1}{2},k+q}] \tag{13}$$

where $|\mathcal{V}_r|$ denotes the cell area, $|\Gamma|$ is an edge length, and the averages μ_1 and μ_2 are defined with the same formulas as for a Cartesian mesh. Note that the discrete residual approximation (13) is a four-point cell vertex. Consequently, it is truly second-order accurate for any quadrangle cell.

Λ Operator

We now apply the Λ operator containing the numerical dissipation to the residual $\tilde{r}$. The result is defined at the cell centers (j, k) and is used in Eq. (12) to advance the conservative variables. For the sake of accuracy, the control cells $\mathcal{V}_{j,k}$ are not exactly the cells of the original mesh, but those for which the nodes are the centers $(j + \frac{1}{2}, k + \frac{1}{2})$ of the staggered cells (see Fig. 2). On the quadrangle cell $\mathcal{V}_{j,k}$ with boundary

$$(\Gamma)_{j+1,k+\frac{1}{2}} \cup (\Gamma)_{j,k+\frac{1}{2}} \cup (\Gamma)_{j+\frac{1}{2},k+1} \cup (\Gamma)_{j+\frac{1}{2},k}$$

the $\Lambda\tilde{r}$ term is defined as

$$(\Lambda\tilde{r})_{j,k} = (\mu_1\mu_2\tilde{r})_{j,k}$$
$$- \frac{1}{2|\mathcal{V}|_{j,k}} \sum_{q=0}^{1} [(h|\Gamma|\Phi_n\mu_2\tilde{r})_{j-\frac{1}{2}+q,k} + (h|\Gamma|\Phi_n\mu_1\tilde{r})_{j,k-\frac{1}{2}+q}] \tag{14}$$

where $|\mathcal{V}|$ denotes the cell areas, $|\Gamma|$ is an edge length, and h is the distance between the centers of the two cells adjacent to an edge. The dissipation matrix Φ_n is defined normally to the edge Γ as

$$\Phi_n = T_{A_n} \mathrm{diag}[\varphi_n^{(i)}] T_{A_n}^{-1}, \qquad \varphi_n^{(i)} = \mathrm{sgn}(a_n^{(i)})\varphi^{(i)},$$
$$\varphi_n^{(i)} = \min\left(1, \frac{|\Gamma|}{h}\frac{|a_n^{(i)}|}{\rho(A_\Gamma)}\right)$$

where A_n is the Jacobian matrix of the flux in the normal direction to the edge Γ, T_{A_n} is a matrix diagonalizing A_n, and the real values $a_n^{(i)}$ and $\varphi_n^{(i)}$ denote the ith eigenvalues of A_n and Φ_n, respectively. Finally, $\rho(A_\Gamma)$ is the spectral radius of the flux Jacobian matrix in the direction of the edge Γ.

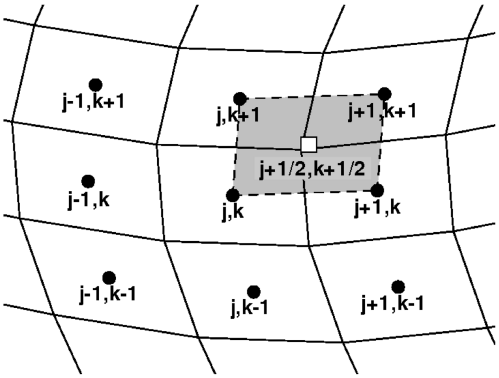

a) Staggered cell $(\mathcal{V}_r)_{j+\frac{1}{2},k+\frac{1}{2}}$ with center $\left(j+\frac{1}{2}, k+\frac{1}{2}\right)$ used to compute the residual $\tilde{r}$

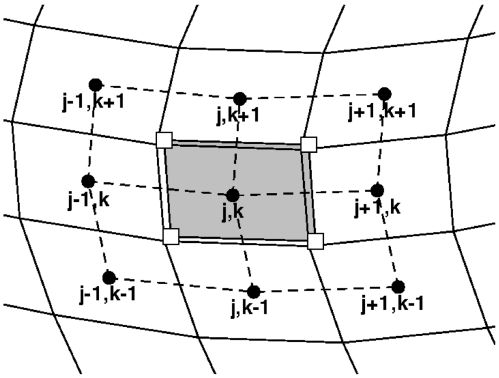

b) Cell $\mathcal{V}_{j,k}$ used to compute $(\Lambda\tilde{r})_{j,k}$

Fig. 2 Curvilinear mesh definition.

Dissipation Properties of the RBV2 Scheme

The RBV2 scheme is fully implicit in time and unconditionally stable. Nevertheless, in the case of diagonal flows, it does not dissipate the shortest-wavelength perturbations in the crosswise direction. To dissipate those spurious wavelengths without altering the vorticity-preserving property of the RBV2 scheme, spatial filters [2] of very-high-order accuracy (10th order) are applied on the conservative variables.

Vortex-Flow Computations

As a first assessment of the vorticity-preserving capability of the RBV2 scheme, computations of a stationary vortex and of a vortex advected at constant speed are presented in this section. The RBV2 solution will be compared with the results given by a classical scheme: the centered scheme with artificial viscosity proposed by Jameson et al. [32], coupled with the same implicit time integration [31] as for RBV2. Both schemes are second-order-accurate in time and space. For the Jameson et al. [32] scheme, we use the standard artificial-viscosity coefficients in all of the computations (including the forthcoming airfoil–vortex interaction): $k_2 = 1/4$ and $k_4 = 1/32$.

Stationary Vortex

We consider the vortex proposed by Yee et al. [33] This vortex is located at $x = y = 0$ at time $t = 0$ and its velocity components u, v, and the temperature T are defined in nondimensional form as

$$\begin{cases} (u, v) = \frac{\Gamma}{2\pi}\exp\left(\frac{1-r^2}{2}\right)(-y, x) \\ T = 1 - \frac{(\gamma-1)\Gamma^2}{8\gamma\pi^2}\exp(1-r^2) \end{cases} \tag{15}$$

where $r^2 = x^2 + y^2$. The entropy is uniform and so the density is $\rho = T^{1/(\gamma-1)}$. The vortex strength is $\Gamma = 5$ and the specific heat ratio is $\gamma = 1.4$. This vortex is a steady solution of the Euler equations. The present test case consists of solving the unsteady Euler equations using the preceding vortex as the initial condition. The observed evolution is due uniquely to the numerical errors. The computational domain extends from -5 to 5 in the x and y directions. Periodic boundary conditions are applied in both directions. A regular Cartesian grid is used with 50×50 cells ($h = \delta x = \delta y = 0.2$) and the time step is $\Delta t = 1$. The computational domain and the initial vorticity field are displayed in Fig. 3.

The vorticity fields of the RBV2 and Jameson et al. [32] scheme (referred to as the conventional scheme) are compared at time $t = 500$ and 1000 in Fig. 4. As with nearly all the schemes, the Jameson et al. scheme diffuses the vorticity field in a long time simulation. The RBV2 scheme preserves the initial vorticity perfectly. The distributions of the pressure and swirl velocity shown in Fig. 5 confirm the remarkable preservation of the stationary vortex by RBV2. It is worthy of note that this result can be obtained for any choice of Δt and does not depend on the vortex considered.

Advected Vortex

We now consider the preceding vortex advected at constant velocity $\mathbf{V_0}$ of components $u_0 = 0.5$ and $v_0 = 0$. The initial conditions are unchanged except the u velocity now augmented with u_0. We use the same computational domain, periodic boundary conditions, and grid.

The problem to solve is now unsteady. Again, the spatial approximation of the RBV2 does not produce any dissipation in the discrete form of the vorticity Eq. (10). The new feature is that the unsteady term $\partial_t\Omega$ is no longer null. In the discrete form of Eq. (10), $\partial_t\Omega$ is discretized with the same implicit three-time-level formula as is $\partial_t w$ in the scheme. This time discretization can produce some dispersive and dissipative errors on the discrete vorticity, depending on the time step used. To assess its influence on the numerical solution, we compare the RBV2 and the conventional scheme for three different time steps presented in Table 1 with the corresponding CFL numbers, for which

$$\mathrm{CFL} = \frac{\Delta t}{h}\max_{j,k}(|\mathbf{V}| + a)^{n=0}_{j,k}$$

where $\mathbf{V}$ is the advection velocity and a is the local sound speed.

Figure 6 shows the vorticity fields at time $t = 100$ for the three time steps. At this time, the vortex should be located at the center of the computational domain. The shift (depending on the rotation direction) with respect to this exact location is due to numerical errors. For the three time steps, RBV2 gives a better vorticity field (compared with the initial condition presented in Fig. 3) with a more accurate vorticity location and a better capture of the vorticity peak.

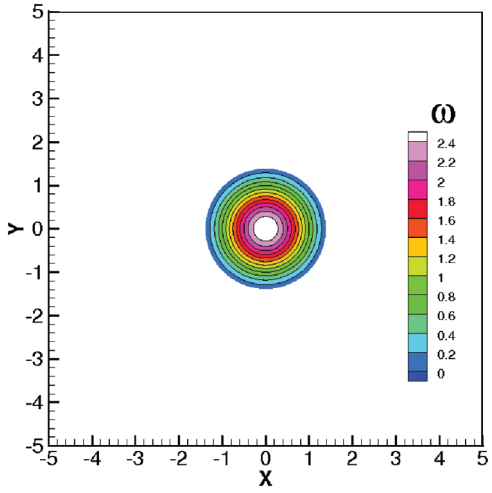

Fig. 3 Computational domain and vorticity field at time $t = 0$.

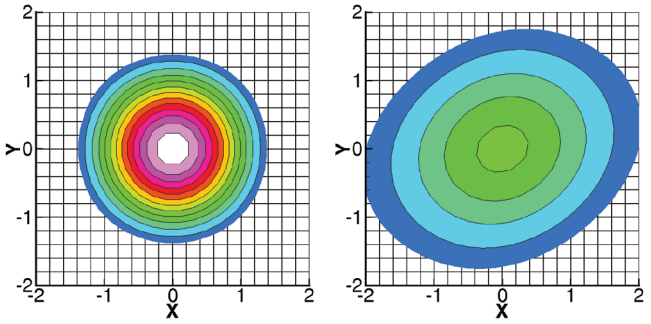

Fig. 4 Numerical evolution of a stationary vortex; vorticity fields of RBV2 and the conventional scheme [31].

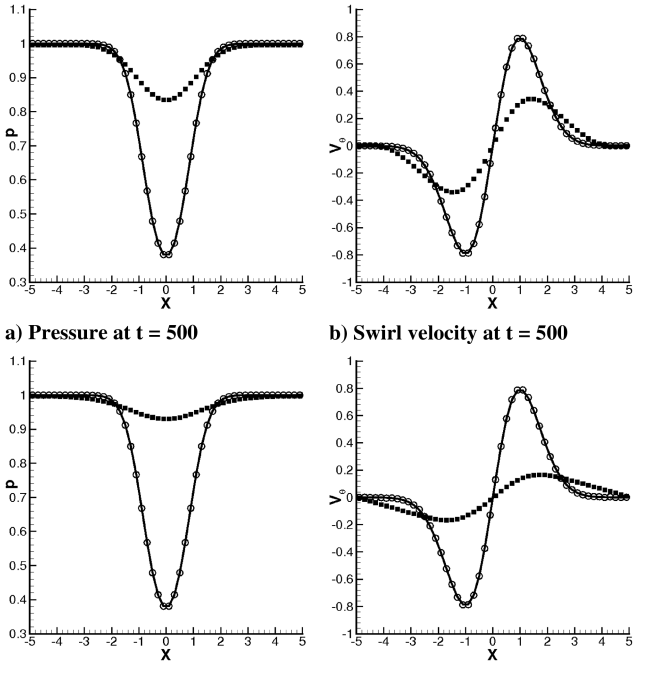

Fig. 5 Evolution of a stationary vortex; pressure and swirl velocity distributions of the exact solution (solid line), RBV2 (○), and conventional scheme [31] (■).

A similar conclusion can be drawn from the pressure and swirl velocity plots displayed in Fig. 7: the RBV2 pressure and velocity profiles are closer to the exact solution.

As mentioned earlier, a good choice for the time step of RBV2 is around $h/(2|\mathbf{V_0}|)$, corresponding here to CFL = 2.42. In practice, the average advection velocity is often known and it may be possible with the present implicit method to keep close to this criterion for vortex propagation over long distances.

Table 1 Time steps and CFL numbers for the advected vortex problem

Δt	$\Delta t\|\mathbf{V_0}\|/h$	CFL number
0.1	0.25	1.21
0.2	0.5	2.42
0.3	0.75	3.63

Application to Airfoil–Vortex Interaction

The RBV2 scheme is applied to an airfoil–vortex interaction taken from the experiments by Lee et al. [23,24], often used to assess the accuracy of numerical simulations (see [23–28]). These experiments reproduce the subsonic head-on parallel interaction of a vortex with a NACA0012 airfoil. The vortex is generated by the diffraction of a shock wave on a NACA0018 airfoil inclined by 30 deg. The NACA0012 airfoil used for the interaction is placed downstream of the vortex generator, in the path of the vortex. Detailed measurements of the initial vortex and unsteady surface-pressure coefficients C_p on the upper and lower sides of the airfoil are given in [23,24].

Initial Conditions and Computational Grids

According to the experimental measurements, the Scully vortex model is chosen for the numerical simulation. In polar coordinates

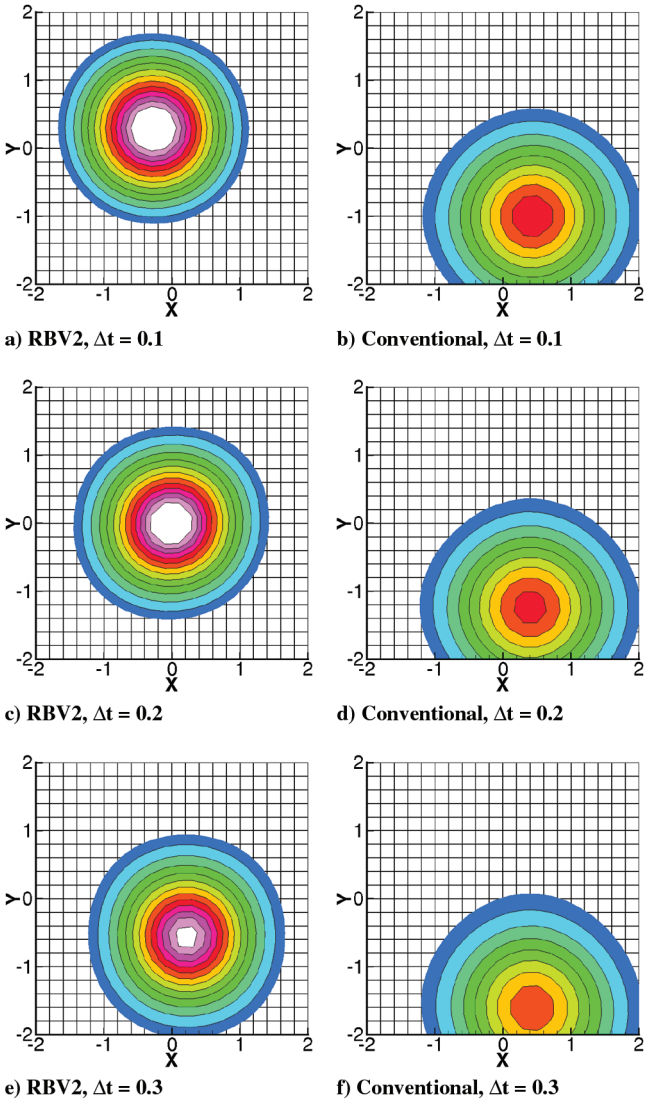

Fig. 6 Horizontal advection of a vortex; vorticity fields at $t = 100$ of RBV2 and the conventional scheme [31] computed with three different time steps.

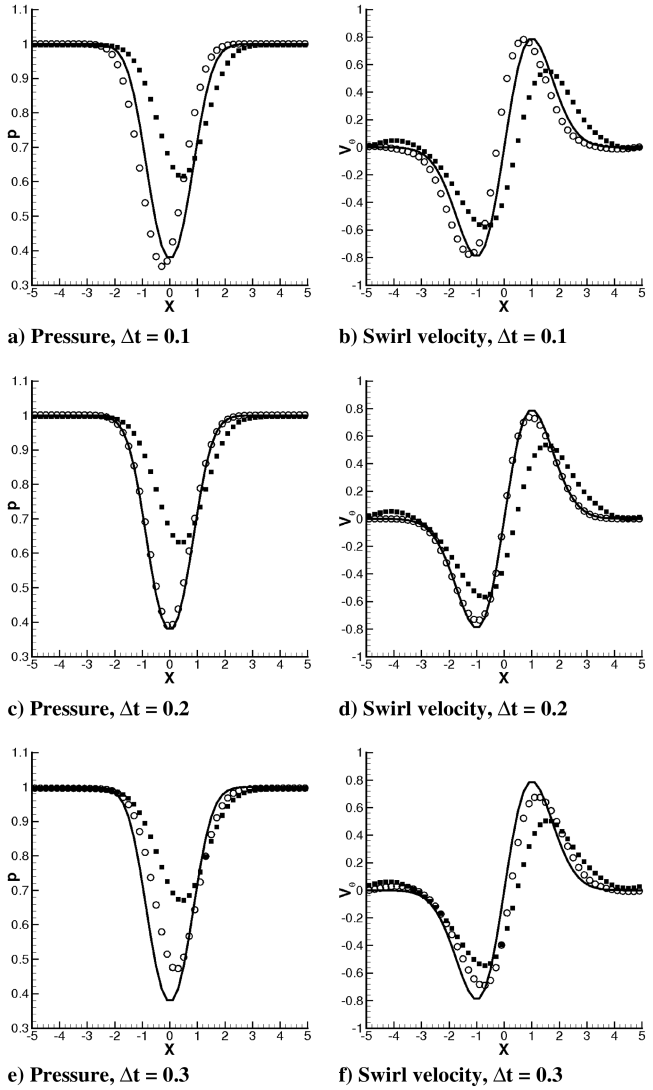

Fig. 7 Horizontal advection of a vortex; pressure and swirl velocity distributions at time $t = 100$ of the exact solution (solid line), RBV2 (○), and conventional scheme [31] (■) computed with three different time steps.

(r, θ), the analytical expression of the tangential velocity v_θ of this vortex is given by

$$v_\theta = \frac{\Gamma}{2\pi r}\left(\frac{r^2}{r^2 + r_0^2}\right) \tag{16}$$

where r_0 is the core radius of the vortex and Γ its circulation.

Because the experimental vortex was generated by a shock diffraction, the pressure and density are not calculated from an isentropic relation, but from the hypothesis of homogeneous enthalpy, γ being the specific heat ratio,

$$\frac{\gamma}{\gamma - 1}\frac{p}{\rho} + \frac{v_\theta^2}{2} = \frac{\gamma}{\gamma - 1}\frac{p_\infty}{\rho_\infty} \tag{17}$$

and from the radial momentum equation

$$\frac{\mathrm{d}p}{\mathrm{d}r} = \frac{\rho v_\theta^2}{r} \tag{18}$$

leading to the ordinary differential equation:

$$\frac{\mathrm{d}p}{p} = \frac{2\gamma\rho_\infty}{2\gamma p_\infty - (\gamma - 1)\rho_\infty v_\theta(r)^2}\frac{v_\theta(r)^2}{r}\,\mathrm{d}r \tag{19}$$

The integration of Eq. (19) provides the analytical expression of the vortex pressure:

$$p(r) = p_\infty \exp\left[\frac{1}{K_2}\left(\frac{\Gamma}{2\pi}\right)^2\left(\arctan\left(\frac{2}{K_2}\frac{p_\infty}{\rho_\infty}(r^2 + r_0^2) - \frac{K_1^2}{K_2}\right) - \frac{\pi}{2}\right)\right] \tag{20}$$

where

$$K_1 = \left(\frac{\gamma - 1}{2\gamma}\right)^{1/2}\frac{\Gamma}{2\pi}, \qquad K_2 = K_1\left(4r_0^2\frac{p_\infty}{\rho_\infty} - K_1^2\right)^{1/2}$$

The preceding vortex is introduced in a steady flow over a NACA0012 airfoil at freestream Mach number $M_\infty = 0.5$ and zero incidence. This steady flow was previously computed using the RBV2 scheme. At time $t = 0$, the vortex is located on the airfoil axis, 3.5 chord lengths ahead of the leading edge, as shown by the initial density contours in Fig. 8. Denoting the freestream velocity as U_∞ and the airfoil chord length as c, the experimental vortex parameters are $\Gamma/(U_\infty c) = -0.283$ and $r_0/c = 0.018$. Note that the vortex is clockwise.

To study grid convergence, a series of four H grids with increasing refinement were generated. For each grid, the computational domain boundary is located 20 chord lengths away from the airfoil. The H topology allows the grid to be Cartesian in most of the upstream excursion of the vortex. Nevertheless, strong grid irregularities arise near the leading edge (see Fig. 9). The spatial steps in the Cartesian region vary from $h = 0.02$ to 0.0025, depending on the computational grid, so that the core of the initial vortex is discretized on 2, 4, 8, and 16 cells, respectively, on the coarse, medium, fine, and very fine grids. The different grid characteristics are summarized in Table 2.

Analysis of the Flow Solution

The solution used for the flow analysis was computed with the RBV2 scheme in the very fine grid using the time step given by Eq. (8) with $|\mathbf{V_0}| = U_\infty$. This ensures that the vortex is very well preserved during its advection and reaches the airfoil with its full strength.

As the clockwise vortex approaches the airfoil (see the streamlines and the density field at different times in Fig. 10), a downward component of the velocity appears at the leading edge of the airfoil and the stagnation point moves upward. As the vortex comes very close to the airfoil, the induced velocity generates a supersonic pocket at the lower side during a short time and a curved shock appears. A secondary counterclockwise vortex is then created just downstream of the curved shock. The conclusions of the first

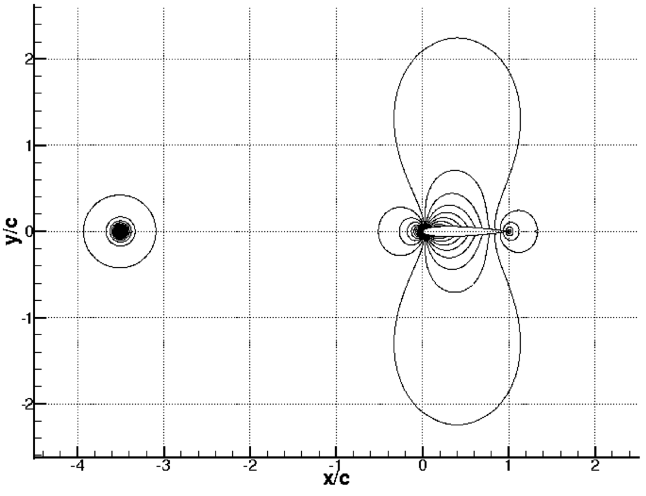

Fig. 8 Density contours at time $t = 0$.

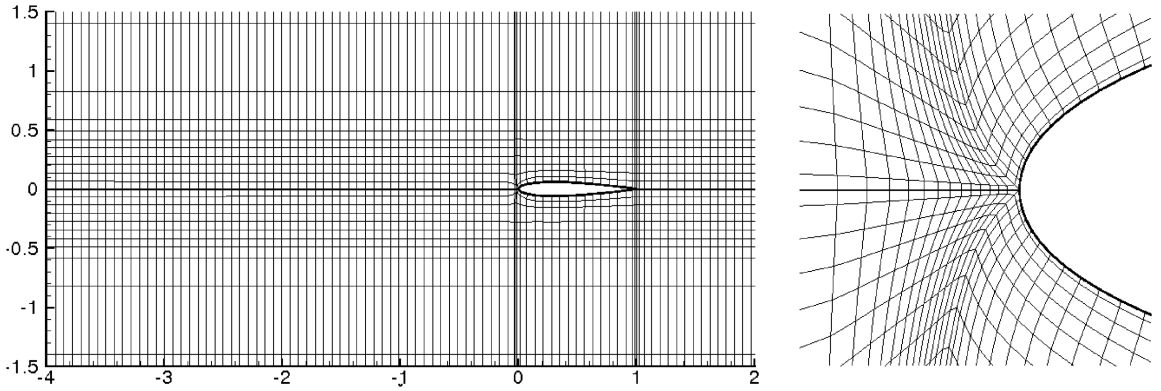

a) H-grid topology b) Leading edge

Fig. 9 Partial views of the H grid for the airfoil–vortex interaction.

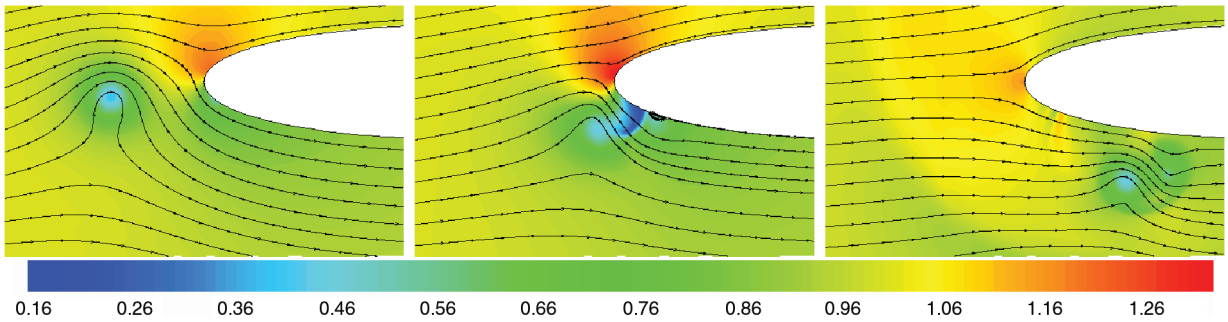

Fig. 10 Streamlines and density field at times $t = 3.45$ (left), 3.55 (center), and 3.65 (right) during the interaction.

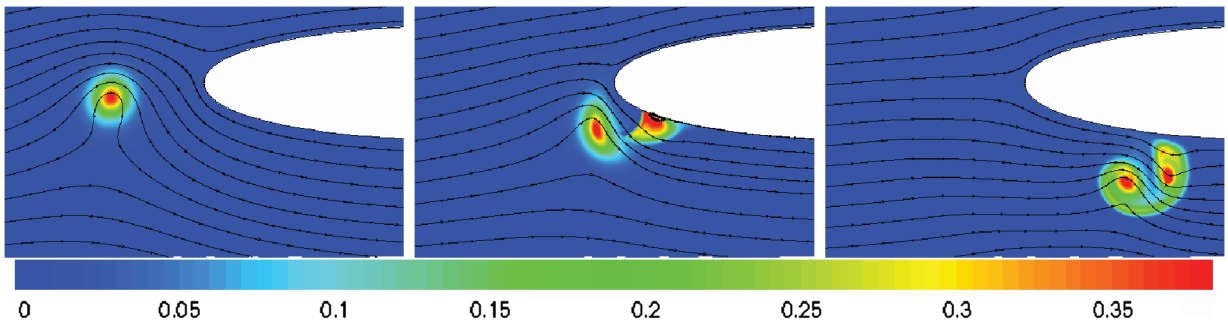

Fig. 11 Streamlines and entropy field at times $t = 3.45$ (left), 3.55 (center), and 3.65 (right) during the interaction.

computations of this airfoil–vortex interaction, made with a thin-layer Navier–Stokes code [23,24], were that viscosity played a significant role in the impact, due to the formation of this secondary vortex related to a flow separation. Nevertheless, later studies [25,26,28] using the Euler equations were able to reproduce the secondary-vortex generation. For classical schemes, this vorticity production could be related to the numerical viscosity or dissipation, but this is not the case for the RBV2 scheme, because the numerical viscosity does not play any role in the vorticity discrete equation. Considering the full Euler equations, the curved shock wave appearing shortly on the lower side seems to be the only phenomenon able to create vorticity in the flow through an alteration of the baroclinic term due to entropy production. This explanation is confirmed by the entropy-deviation fields ($\mathrm{d}S = (S - S_\infty)/S_\infty$) displayed in Fig. 11.

After the vortex pair has moved downstream, the stagnation point comes back to its initial position and acoustic waves occur. They are typical of the blade–vortex-interaction noise for a helicopter rotor blade. More precisely, during the stagnation-point return, a compressibility wave is generated by the detachment of the high-pressure region on the upper side near the leading edge (see the red lob in the acoustic pressure field in Fig. 12). At the same time, the supersonic pocket leaves the lower side of the airfoil and generates a transonic wave (blue lob in Fig. 12). A second compressibility wave

Table 2 Parameters for the grid convergence study

Grid name	Number of cells	Cartesian-region step size	Points in vortex core	Time step	$\mathrm{CFL}_{\max}$
Coarse	48,000	0.02	2	0.01	2.73
Medium	144,000	0.01	4	0.005	3.97
Fine	397,000	0.005	8	0.0025	4.73
Very fine	1,350,000	0.0025	16	0.00125	5.23

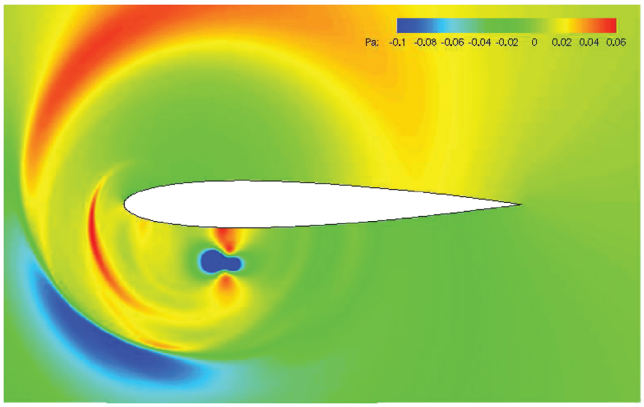

Fig. 12 Acoustical pressure field at time $t = 3.75$.

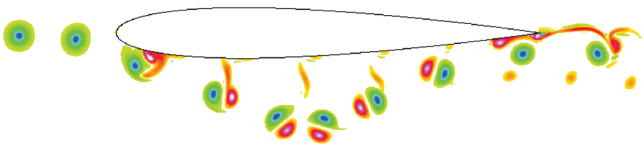

Fig. 13 Vorticity snapshots at successive times around the airfoil; initial negative vortex is in blue and green; the generated positive vortex is in red and white; the RBV2 solution is in the very fine grid.

arises on the lower side. This third wave, already noticed in [28], comes from the detachment of a high-pressure region appearing downstream of the shock after the formation of the secondary vortex.

The trajectories of the vortices during and after the first impact are presented in Fig. 13. After this impact, the vortex pair moves away from the airfoil and starts a clockwise rotation. When it reaches a position corresponding to the middle of the chord, the vortex pair keeps on its rotation but comes back to the airfoil until the secondary vortex collides with the wall in the trailing-edge region. At the end of the computation, the vortex is almost as strong as before the interaction and keeps a trajectory very close to its initial direction.

The time evolution of the pressure on the upper and lower sides of the airfoil is shown in Fig. 14; the present results are compared with the experiments [24] and previously published Euler computations using either compressible vorticity confinement [28] or mesh adaption in a structured [25] or unstructured [26] way. On the upper side, the RBV2 results well match the experiments and most of the previous computations. On the lower side, the agreement between the computations is similar, but the pressure loss occurring at the beginning of the interaction is overestimated with respect to the experimental data. This transitory failure could be cured by including the viscous effects in the simulation (see [23,27,28]).

Grid Convergence of RBV2 Versus a Conventional Scheme

To assess the contribution of the vorticity-preserving approach, a convergence study is now performed using RBV2 and the conventional scheme [31]. The computations are carried out on the coarse, medium, and fine meshes with the parameters defined in Table 2. Because the problem is unsteady, the grid convergence should also concern the time discretization. The time step is decreased in the same ratio as the space step in the Cartesian region. The maximal CFL number is reached near the airfoil and is slightly varying with the mesh, because the refinement is not purely homothetic.

Figure 15 compares the time history of the pressure coefficients obtained by RBV2 and the conventional scheme on the three meshes. Clearly, the grid convergence to the Euler solution is faster with RBV2 than with the conventional scheme. Actually, the pressure on both sides is well-predicted by RBV2 on all grids except the coarser grid, containing only two points in the vortex core.

Both schemes give a similar airfoil pressure distribution in the fine grid at the beginning of the interaction. Nevertheless, in some real flow problems, vortex trajectories play a significant role: for instance, for the blade–vortex and blade–wake interactions in helicopter-rotor flows. For this reason, it is necessary to check that grid convergence is not only reached on the pressure but also on the vortex trajectories after the interaction. As shown in Fig. 16, the vortex trajectories and deformations are considerably dependent on the scheme and grid used for the computation. The RBV2 solution computed in the fine grid (containing eight points in the vortex core) is the only one to closely reproduce the trajectories and deformations of the reference solution shown in Fig. 13 (obtained with 16 points in the vortex core). The solution given by the conventional scheme in the fine grid is very similar to the RBV2 solution in the medium grid.

Conclusions

In this paper, a new vorticity-preserving scheme (RBV2) for solving the compressible Euler equations was extended to curvilinear grids and applied to the interaction between a Scully vortex and a NACA0012 airfoil to assess its capabilities. A grid convergence study and comparisons with a conventional scheme on the same meshes have revealed the gains due to the vorticity preservation feature of the new scheme.

A major improvement of the RBV2 scheme lies in the representation of the trajectory and deformation of the vortex during the airfoil–vortex interaction. For a given accuracy, the RBV2 scheme allows the use of half of the points (in each direction) needed by a conventional scheme.

Three-dimensional computations should now be done to check whether this trend is confirmed in more realistic applications. Let us simply note that the theoretical grounds were stated; that is, the RBV2 scheme has been proved [21] to be vorticity-preserving for the 3-D Euler equations.

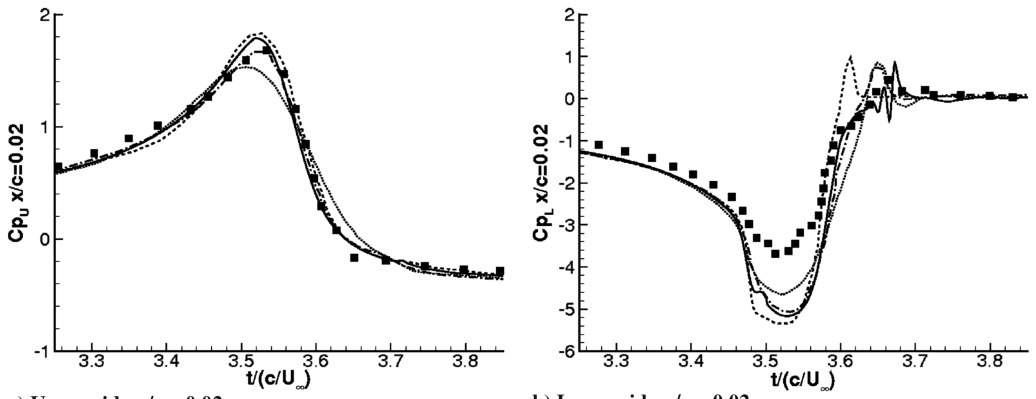

a) Upper side x/c = 0.02 b) Lower side x/c = 0.02

Fig. 14 Time history of the pressure coefficients at $x/c = 0.02$ during the airfoil–vortex interaction; comparison of experimental data [24] (■) and inviscid computations using RBV2 (solid line), structured adaptive mesh refinement method [25] (dashed-dotted line), unstructured adaptive mesh refinement method [26] (dashed line), and compressible vorticity confinement method [28] (dotted line).

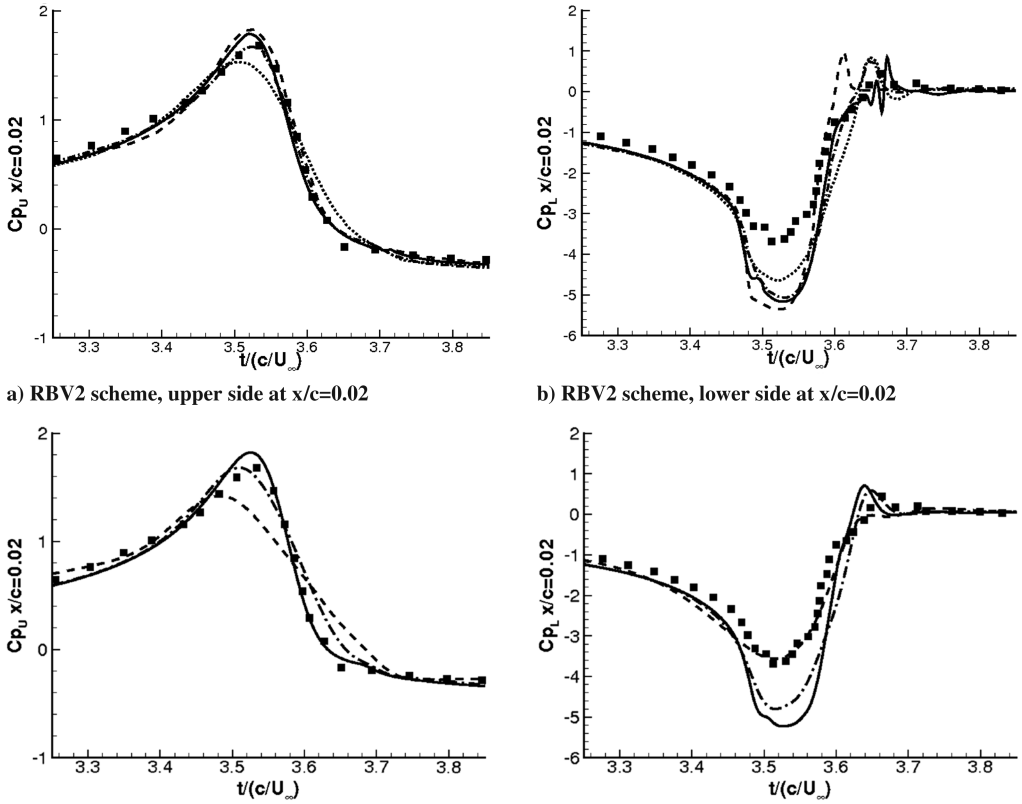

a) RBV2 scheme, upper side at x/c=0.02

b) RBV2 scheme, lower side at x/c=0.02

c) Conventional scheme, upper side at x/c=0.02

d) Conventional scheme, lower side at x/c=0.02

Fig. 15 Time history of the pressure coefficients at $x/c = 0.02$ during the airfoil–vortex interaction; comparison of experimental data [24] (■) and inviscid computations using RBV2 and a conventional scheme [31]; solutions in the coarse grid (dashed line), medium grid (dashed-dotted line), and fine grid (solid line).

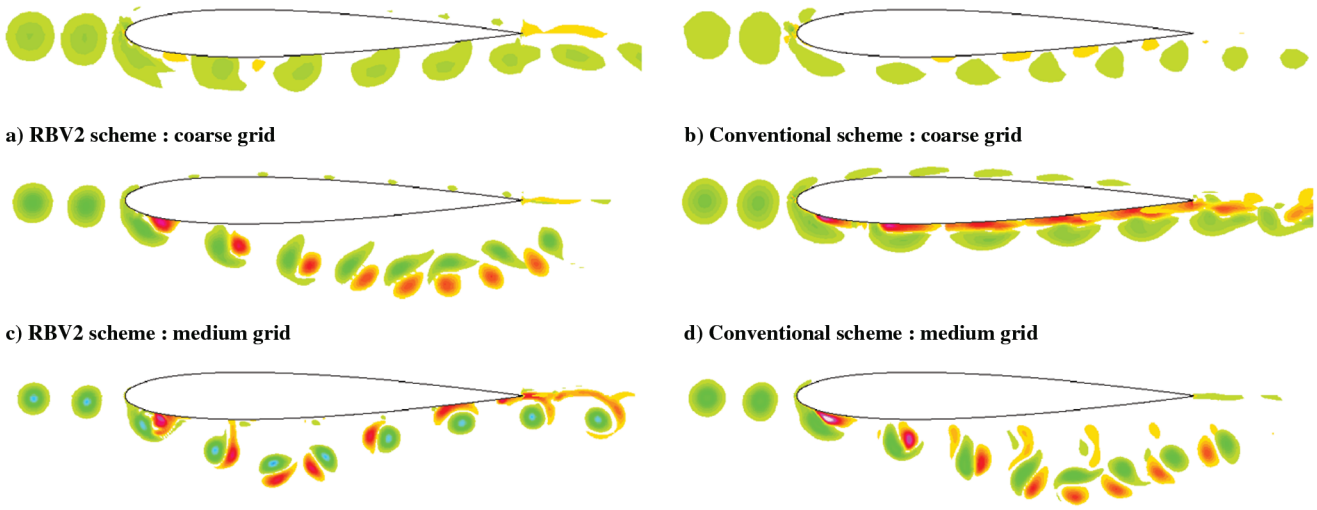

a) RBV2 scheme : coarse grid

b) Conventional scheme : coarse grid

c) RBV2 scheme : medium grid

d) Conventional scheme : medium grid

e) RBV2 scheme : fine grid

f) Conventional scheme : fine grid

Fig. 16 Vorticity snapshots at successive times around the airfoil during the interaction; grid convergence for RBV2 and the conventional scheme [31].

References

[1] Bogey, C., and Bailly, C., "A Family of Low Dispersive and Low Dissipative Explicit Schemes for Flow and Noise Computations," *Journal of Computational Physics*, Vol. 194, No. 1, 2004, pp. 194–214. doi:10.1016/j.jcp.2003.09.003

[2] Lele, S. K., "Compact Finite Difference Schemes with Spectral-Like Resolution," *Journal of Computational Physics*, Vol. 103, No. 1, 1992, pp. 16–42. doi:10.1016/0021-9991(92)90324-R

[3] Visbal, M. R., and Gaitonde, D. V., "High-Order-Accurate Methods for Complex Unsteady Subsonic Flows," *AIAA Journal*, Vol. 37, No. 10, 1999, pp. 1231–1239.

[4] Visbal, M. R., and Gaitonde, D. V., "On the Use of High-Order finite Difference Schemes on Curvilinear and Deforming Meshes," *Journal of Computational Physics*, Vol. 181, No. 1, 2002, pp. 155–185. doi:10.1006/jcph.2002.7117

[5] Lerat, A., and Corre, C., "A Residual-Based Compact Scheme for the Compressible Navier-Stokes Equations," *Journal of Computational Physics*, Vol. 170, No. 2, 2001, pp. 642–675. doi:10.1006/jcph.2001.6755

[6] Lerat, A., and Corre, C., "Residual-Based Compact Schemes for Multidimensional Hyperbolic Systems of Conservation Laws,"

Computers and Fluids, Vol. 31, No. 4, 2002, pp. 639–661.
doi:10.1016/S0045-7930(01)00075-5

[7] Corre, C., Hanss, G., and Lerat, A., "A Residual-Based Compact Scheme for the Unsteady Compressible Navier-Stokes Equations," *Computers and Fluids*, Vol. 34, Nos. 4–5, 2005, pp. 561–580.
doi:10.1016/j.compfluid.2003.08.003

[8] Corre, C., Falissard, F., and Lerat, A., "High-Order Residual-Based Compact Schemes for Compressible Inviscid Flows," *Computers and Fluids*, Vol. 36, No. 10, 2007, pp. 1567–1582.
doi:10.1016/j.compfluid.2007.03.010

[9] Harten, A., and Osher, S., "Uniformly High-Order Accurate Nonoscillatory Schemes," *SIAM Journal on Numerical Analysis*, Vol. 24, No. 2, 1987, pp. 279–309.
doi:10.1137/0724022

[10] Harten, A., Engquist, B., Osher, S., and Chakravarthy, S., "Uniformly High Order Essentially Nonoscillatory Schemes," *Journal of Computational Physics*, Vol. 71, No. 2, 1987, pp. 231–303.
doi:10.1016/0021-9991(87)90031-3

[11] Shu, C. W., and Osher, S., "Efficient Implementation of Essentially Nonoscillatory Shockcapturing Schemes," *Journal of Computational Physics*, Vol. 77, No. 2, 1988, pp. 439–471.
doi:10.1016/0021-9991(88)90177-5

[12] Jiang, G. S., and Shu, C. W., "Efficient Implementation of Weighted ENO Schemes," *Journal of Computational Physics*, Vol. 126, No. 1, 1996, pp. 202–228.
doi:10.1006/jcph.1996.0130

[13] Balsara, D. S., and Shu, C. W., "Monotonicity Preserving Weighted Essentially Nonoscillatory Schemes with Increasingly High-Order of Accuracy," *Journal of Computational Physics*, Vol. 160, No. 2, 2000, pp. 405–452.
doi:10.1006/jcph.2000.6443

[14] Lesaint, P., and Raviart, P. A., "On a Finite Element Method for Solving The Neutron Transport Equation," *Mathematical Aspects of Finite Elements in Partial Differential Equations*, Academic Press, New York, 1974, pp. 89–123.

[15] Johnson, C., and Pitkäranta, J., "An Analysis of the Discontinuous Galerkin Method for a Scalar Hyperbolic Equation," *Mathematics of Computation*, Vol. 46, Jan. 1986, pp. 1–26.
doi:10.2307/2008211

[16] Allmaras, S., and Giles, M. B., "A Second-Order Flux Split Scheme for the Unsteady 2-D Euler Equations on Arbitrary Meshes," AIAA Paper 87-119, 1987.

[17] Berde, B., and Borrel, M., "Comparison of Higher-Order Godunov-Type Schemes for the Euler Equations on Irregular Meshes," *ECCOMAS Computational Fluid Dynamics Conference*, Wiley, New York, 1994, pp. 288–295.

[18] Bassi, F., and Rebay, S., "A High-Order Accurate Discontinuous Finite Element Method for the Numerical Solution of the Compressible Navier-Stokes Equations," *Journal of Computational Physics*, Vol. 131, No. 2, 1997, pp. 267–279.
doi:10.1006/jcph.1996.5572

[19] Cockburn, B., and Shu, C. W., "The Runge-Kutta Discontinuous Galerkin Method for Conservation Laws, 5: Multidimensional Systems," *Journal of Computational Physics*, Vol. 141, No. 2, 1998, pp. 199–224.
doi:10.1006/jcph.1998.5892

[20] Morton, K. W., and Roe, P. L., "Vorticity-Preserving Lax-Wendroff-Type Scheme for the System Wave Equation," *SIAM Journal on Scientific Computing*, Vol. 23, No. 1, 2001, pp. 170–192.
doi:10.1137/S106482759935914X

[21] Lerat, A., Falissard, F., and Sidés, J., "Vorticity-Preserving Schemes for the Compressible Euler Equations," *Journal of Computational Physics*, Vol. 225, No. 1, 2007, pp. 635–651.
doi:10.1016/j.jcp.2006.12.025

[22] Scully, M. P., "Computation of Helicopter Rotor Wake Geometry and Its Influence on Rotor Harmonic Loads," Massachusetts Inst. of Technology, TR ASRL TR-178-1, Cambridge, MA, 1975.

[23] Lee, S., and Bershader, D., "Head-On Parallel Blade-Vortex Interaction," *AIAA Journal*, Vol. 32, No. 1, 1994, pp. 16–22.

[24] Lee, S., Bershader, D., and Rai, M. M., "An Experimental and Computational Study of 2-D Parallel Blade-Vortex Interaction,"AIAA Paper 91-3277, 1991.

[25] Tang, L., and Baeder, J. D., "Adaptive Euler Simulations of Airfoil—Vortex Interaction," *International Journal for Numerical Methods in Fluids*, Vol. 53, No. 5, 2007, pp. 777–792.
doi:10.1002/fld.1306

[26] Oh, W. S., Kim, J. S., and Kwon, O. J., "Numerical Simulation of Two-Dimensional Blade-Vortex Interactions Using Unstructured Adaptive Meshes," *AIAA Journal*, Vol. 40, 2002, pp. 474–480.

[27] Oh, W. S., Kim, J. S., and Kwon, O. J., "Time-Accurate Navier-Stokes Simulation of Vortex Convection Using an Unstructured Dynamic Mesh Procedure," *Computers and Fluids*, Vol. 32, No. 5, 2003, pp. 727–749.
doi:10.1016/S0045-7930(02)00015-4

[28] Morvant, R., Badcock, K. J., Barakos, G. N., and Richards, B. E., "Airfoil-Vortex Interaction Using the Compressible Vorticity Confinement Method," *AIAA Journal*, Vol. 43, No. 1, 2005, pp. 63–75.
doi:10.2514/1.5177

[29] Huang, Y. and Lerat, A., "Second-Order Upwinding Through a Characteristic Time- Step Matrix for Compressible Flow Calculations," *Journal of Computational Physics*, Vol. 142, No. 2, 1998, pp. 445–472.
doi:10.1006/jcph.1998.5935

[30] Peyret, R., and Taylor, T., *Computational Methods for Fluid Flow*, Springer–Verlag, New York, 1983.

[31] Jameson, A., "Time Dependent Calculations Using Multigrid, with Applications to Unsteady Flows Past Airfoils and Wings," AIAA Paper 91-1596, 1991.

[32] Jameson, A., Schmidt, W., and Turkel, E., "Solutions of the Euler Equations by Finite Volume Methods Using Runge-Kutta Time-Stepping Schemes," AIAA Paper 8l-l259, 198l.

[33] Yee, H. C., Sandham, N. D., and Djomehri, M. J., "Low-Dissipative High-Order Shock-Capturing Methods Using Characteristic-Based Filters," *Journal of Computational Physics*, Vol. 150, No. 1, 1999, pp. 199–238.
doi:10.1006/jcph.1998.6177

D. Gaitonde
Associate Editor